Desalination and Water Treatment
www.deswater.com

doi:10.5004/dwt.2017.21066

83 (2017) 144–158
July

Modeling mercury (II) removal at ultra-low levels from aqueous solution using graphene oxide functionalized with magnetic nanoparticles: optimization, kinetics, and isotherm studies

Mohammad Khazaei[a,b], Simin Nasseri[b,c,*], Mohammad Reza Ganjali[d,e], Mehdi Khoobi[f], Ramin Nabizadeh[b], Amir Hossein Mahvi[b,g], Elham Gholibegloo[h], Shahrokh Nazmara[b]

[a]*Research Center for Environmental Pollutants, Qom University of Medical Sciences, Qom, Iran, email: khazaei57@gmail.com (M. Khazaei)*
[b]*Department of Environmental Health Engineering, School of Public Health, Tehran University of Medical Sciences, Tehran, Iran, P.O.Box.: 14155-6446, Tel. +98 2188954914, Fax +98 2188950188, email: maroshani35@gmail.com (S. Nasseri), rnabizadeh@tums.ac.ir (R. Nabizadeh), ahmahvi@yahoo.com (A.H. Mahvi), snazmara@gmail.com (S. Nazmara)*
[c]*Center for Water Quality Research, Institute for Environmental Research, Tehran University of Medical Sciences, Tehran, Iran*
[d]*Center of Excellence in Electrochemistry, Faculty of Chemistry, University of Tehran, Tehran, Iran, email: ganjali@khayam.ut.ac.ir (M.R. Ganjali)*
[e]*Biosensor Research Center, Endocrinology & Metabolism Molecular-Cellular Sciences Institute, Tehran University of Medical Sciences, Tehran, Iran*
[f]*Faculty of Pharmacy and Pharmaceutical Sciences Research Center, Tehran University of Medical Sciences, Tehran, Iran, email: mehdi.khoobi@gmail.com (M. Khoobi)*
[g]*Center for Solid Waste Research, Institute for Environmental Research, Tehran University of Medical Sciences, Tehran, Iran*
[h]*Department of Organic Chemistry, University of Zanjan, Zanjan, Iran, email: elhamgholibegloo@yahoo.com (E. Gholibegloo)*

Received 27 August 2016; Accepted 21 June 2017

ABSTRACT

Magnetic graphene oxide (Fe_3O_4@SiO_2-GO) nanocomposite was fabricated through a facile process and its application was found to be an excellent adsorbent for capturing low concentrations of mercury (II) from water. The effects of four independent factors, including nanocomposite dosage, contact time, pH, and initial mercury ion concentration on the mercury (II) removal were studied, and the process was optimized using response surface methodology (RSM). The optimum values of the variables adsorbent dosage, contact time, pH, and mercury (II) initial concentration were found to be 23 mg L^{-1}, 21 min, 5.5, and 550 ppb, respectively. The adsorbent equilibrium capacity was 328.3 mg g^{-1} after 21 min. By using goodness-of-fit measures (GoFMs), the Sips isotherm was found to provide a good fit with the adsorption data (K_S = 0.388 L mg^{-1}, n_S = 0.44, q_m = 569.3 mg g^{-1}, and R^2 = 0.989). The mean free energy E_{ads} was 11.901 kJ/mol, confirmed chemisorption mechanisms. The kinetic study determined good compliance of experimental data with the double exponential kinetic model (R^2 = 0.997).

Keywords: Graphene oxide; Adsorption; Mercury (II); Response surface methodology; Central composite design; Model

1. Introduction

Mercury ion enters the drinking waters from various sources such as the erosions of natural deposits, the industrial effluents from refineries, electronic products, batteries, landfills leachates, and fossil fuel combustion [1]. Long-term exposure to mercury can cause kidney, brain, eye, and lung damages [1,2]. Maximum contaminant level (MCL) of 2 ppb set by US Environmental Protection Agency (EPA) for mercury ions in drinking water reveals the considerations regarding to the high toxicity of mercury [3].

*Corresponding author.

Most of experiments regarding the removal of water contaminants have emphasized the concentrations generally occurring in the industrial discharges [1,2,4–6] and despite health considerations regarding sub-ppm presence of mercury ions in drinking water, only few studies have focused on the elimination of mercury ions at ppb-levels [7]. However, some methods such as applying functionalized adsorbents, and membrane technologies have been approved for capturing low amounts of mercury ions at ppb-levels occurring in drinking waters [8,9]. Beside the advantages of adsorbents, most of them involves some inherent drawbacks such as low adsorption capacity [10,11], and difficulties due to the separation of saturated adsorbent from water, after ending the adsorption contact time [12]. Graphene oxide (GO), as a carbon-based nonmaterial, shows noticeable adsorptive properties [13,14] and creates highly stable aqueous dispersion [9,15].

Currently, some works have focused on applying Fe_3O_4 nanoparticles as a separator agent to extract the GO dispersions from aqueous solution [9,11]. Conventional methods to attach Fe_3O_4 nanoparticles on GO layers have led to fabricating reduced GO (rGO), simultaneously [16]. The resulted rGO has weak dispersibility due to the elimination of hydroxide and carboxylic groups during chemical reduction [15]. However, sustaining the dispersibility of GO nanosheets having magnetic property is still under investigation [17,18]. Several literatures reported the fabrication of Fe_3O_4/GO without the chemical reduction path via covalent bonds between the GO carboxylic groups and Fe_3O_4nanoparticles [17,19].

This investigation was aimed to synthesize covalently bond Fe_3O_4@SiO_2-GO. The prepared nanostructure is intended to be highly dispersible and easy to separate from water after adsorption process. In addition, the mercury removal process was modeled and the optimal operational condition was determined by applying response surface methodology (RSM). In the ordinary adsorption studies, one factor is changed at a time, whereas the other factors remained constant [20]. RSM, as a statistical method, was applied to determine the correlation between responses derived from experimental runs and the predicted results from the model [21–23].

2. Experimental

2.1. Materials

Graphite powder (particle size < 20 μm), tetraethyl orthosilicate (TEOS), (3-aminopropyl) triethoxysilane (APTES), n-hydroxysuccinimide (NHS), and 1- ethyl-3-(3-dimethyl aminopropyl) carbodiimide (EDC.HCl) were purchased from Sigma-Aldrich, Ltd. Co. All other chemicals such as sodium nitrate ($NaNO_3$), potassium permanganate ($KMnO_4$), sulfuric acid (H_2SO_4), hydrochloric acid (HCl), hydrogen peroxide aqueous solution (H_2O_2), iron chloride hexahydrate ($FeCl_3$, $6H_2O$), and iron chloride tetrahydrate ($FeCl_2$, $4H_2O$) were of reagent grade and used without further purification.

2.2. Preparation of graphene oxide (GO)

Graphene oxide was synthesized from graphite powder using the modified Hummers approach [20,24]. As a brief description, 2.0 g of $NaNO_3$ and 2.0 g of graphite powder were blended by 92 mL of H_2SO_4 (98%) in a flask and mixed in an ice bath for 0.5 h. Then, 12.0 g of $KMnO_4$ was added slowly to the solution. The ice bath was removed after 0.5 h, and then, the solution was stirred in a water bath for 6 h at 35°C. 160 mL of the deionized water was dropped slowly into the flask. Then, the obtained mixture was mixed at 90°C for 2 h. Afterwards, 400 mL of deionized water was added, followed by adding 12 mL H_2O_2 (30%). The color of mixture was, then, turned to bright yellow. Removing metal ions was achieved by washing intermittently with HCl solution (1:10) and deionized water [25]. Exfoliated graphene oxide was obtained by sonication and centrifugation of final dispersed solution [26].

2.3. Preparation of Fe_3O_4@SiO_2-NH_2

The Fe_3O_4 magnetic nanoparticles (Fe_3O_4MNPs) were fabricated by applying coprecipitation method [27]. Fe_3O_4@SiO_2-NH_2 nanocomposite was synthesized by dispersing 1.0 g of Fe_3O_4MNPs into the mixture of EtOH: H_2O (4:1) under the ultrasonic water bath. Then, a mixture of 0.5 mL TEOS and 2 mL $NH_3{\cdot}H_2O$ (25%) was prepared and stirred at 50°C for 6 h. The pasty obtained product was then collected using an external magnetic field, washed with ethanol, and dried under vacuum. 1 g of the obtained Fe_3O_4@SiO_2 was added into 25 mL dried toluene and then treated by the addition of 1 mL APTES [28]. After refluxing the mixture for 24 h under nitrogen atmosphere, the product was washed with ethanol, and then dried at 70°C for 24 h [20].

2.4. Preparation of Fe_3O_4@SiO_2-GO

The condensation reaction between amine groups of Fe_3O_4@SiO_2-NH_2 and carboxyl groups of GO is occurred to prepare Fe_3O_4@SiO_2-GO [20]. Briefly, GO (0.2 g) was dispersed in deionized water (50 mL) containing NHS (0.1 g) and EDC. HCl (0.2 g) under ultra-sonication for 2 h. Then, Fe_3O_4@SiO_2-NH_2 (0.5 g) was added into the mixture and stirred for 12 h at room temperature. The solid pasty product was separated *via* magnetic separation, washed with EtOH/ H_2O, and dried under vacuum for 12 h [19]. A schematic view of the synthesis path can be observed in Fig. 1.

2.5. Characterization

Scanning electron microscopy (SEM) images were recorded with a Hitachi-S4160 scanning microscope. Transmission electron microscopy (TEM) images were prepared on a JEOL-2010 microscope. A Nanoscope V multimode atomic force microscope (Veeco Instruments, USA) was used to perform AFM measurements. The AFM images were taken from samples prepared by deposition of a dispersed GO/methanol solution (70 mg mL^{-1}) onto a fresh mica surface and allowed to dry in air [26]. The images were taken under ambient condition by adjusting the instrument on the tapping mode. Fourier transformed infrared (FTIR) spectra were recorded on a Nicolet Magana-IR 750 spectrometer with KBr pellets at room temperature. The TGA measurement was carried out using a Shimadzu TGA-50

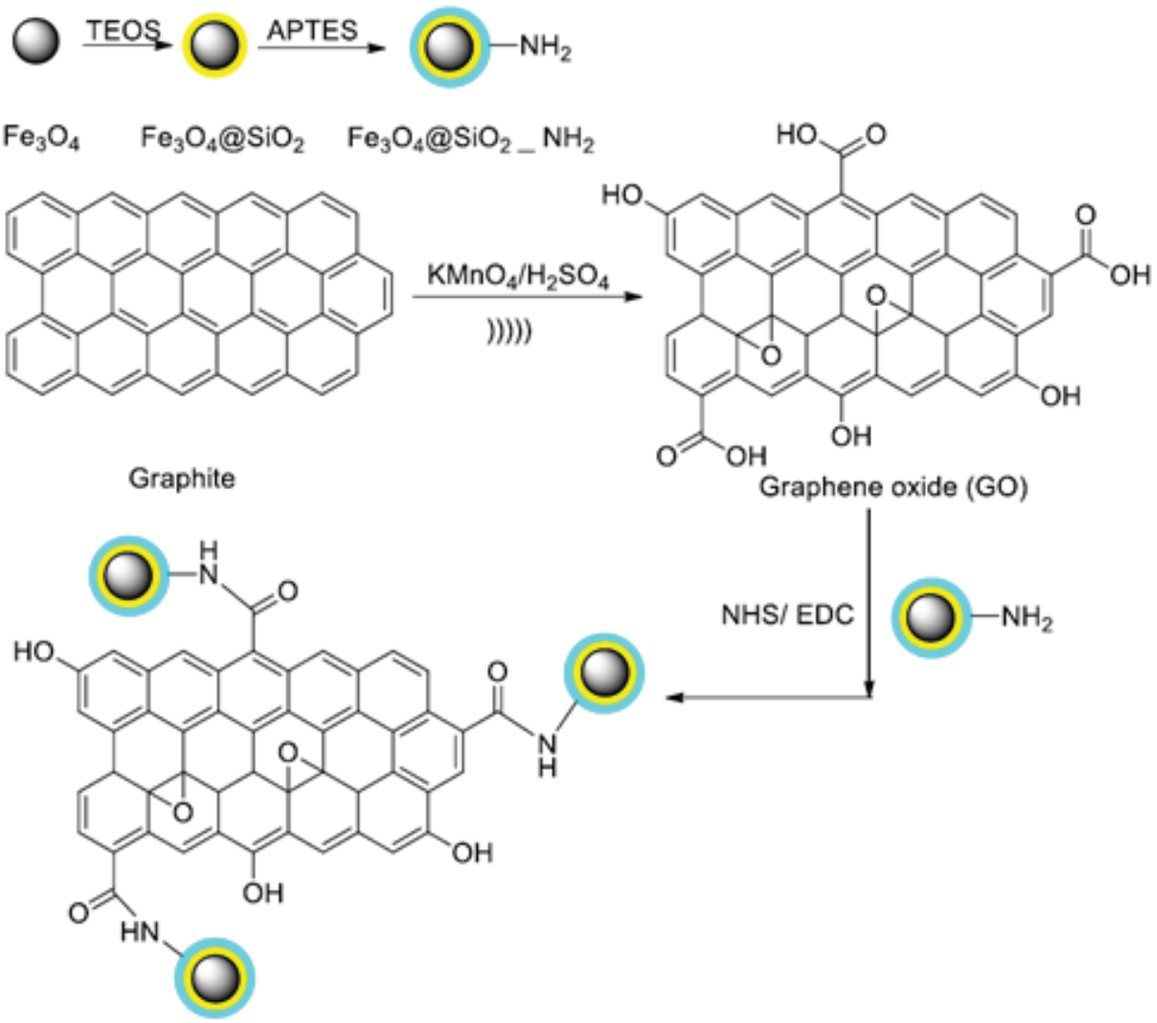

Fig .1. Schematic representation of chemical path to the synthesis of Fe_3O_4@SiO_2-GO nanocomposite. (TEOS: tetraethylorthosilicate, APTES: 3 aminopropyltriethoxysilane).

thermogravimetric analyzer. Magnetic measurements were conducted in a MPMS-XL SQUID magnetometer.

Mercury (II) measurements in the aqueous solution were performed by using a Spectro Arcos ICP-optical emission spectrometer (SPECTRO Analytical Instruments, Kleve, Germany), based on radial plasma observation. The Spectro Arcos has a Paschen–Runge mount equipped with 32 linear CCD detectors. The CCD detectors supply the ability of simultaneous monitoring of line intensities at wavelengths between 130 and 770 nm.

2.6. Batch adsorption experiments

Batch experiments were conducted in Erlenmeyer flasks (100 mL) using a thermostatic shaker (Innova 4340, Eppendorf, Germany). Various volumes included known quantities of Fe_3O_4@SiO_2-GO dispersions were added into 20 mL solution contained Hg^{2+} ion. A constant mixing at 300 rpm was conducted for all experiments. By using an external magnetic field, the adsorbent was separated from the aqueous solution after contact time. Then, the final Hg^{2+} ion concentration was measured and the removal efficiency was determined by using the following equation.

$$R(\%) = \frac{(C_0 - C_e)}{C_0} \times 100 \quad (1)$$

where R (%) is the removal efficiency, C_0 and C_e are the initial and final (as mg L^{-1}) concentrations of Hg^{2+} ion, respectively.

Equilibrium capacity of the nanocomposite was obtained as follows:

$$q_e = \frac{(C_0 - C_e)}{x_{ads}} \quad (2)$$

where q_e is the equilibrium capacity (mg g^{-1}), x_{ads} is the nanocomposite dose in aqueous solution (g L^{-1}).

All the parameters in the kinetic and isotherm models were obtained by non-linear regression by using Solver engine in Microsoft-Excel, 2010.

2.7. Experimental design

Central composite design (CCD) was applied to study the mercury (II) adsorption. The response surface methodology (RSM) was used to determine the combined effects of adsorbent (X_1), contact time (X_2), and initial mercury (II) concentration (X_3) on the removal process. Table 1 shows the original and coded levels of independent variables.

The removal efficiencies of mercury (II) determined by Eq. (1), was considered the output responses (Y).

Table S1 presents the components of all 26 experiments. Two blocks were obtained including one cube block, and one star block. Consequently, total 26 independent experiments were acquired, comprising 12 center points, 2^3 =8 design points, and 2 × 3 = 6 axial points (Table S1). Eq. (3) shows a quadratic model applied to estimate the relationship between three independent variables and the dependent variable (*Y*), which is mercury (II) removal efficiency.

$$Y = b_0 + \sum_{i=1}^{k} b_i X_i + \sum_{i=1}^{k} b_{ii} X_i^2 + \sum_{i=1}^{k-1} \sum_{j=2}^{k} b_{ij} X_i X_j + c \quad (3)$$

where b_0 is a constant value (the intercept), b_i, b_{ii}, and b_{ij} are the coefficients of linear, quadratic, and interactive effects, respectively. X_i, and X_j are the independent variables, c is the error of prediction. The CCD analysis and the statistical analysis, such as ANOVA, F-test, and t-test were done by applying R software (version 3.3.1).

Table 1
The original and coded levels of independent variables

Original factors	Coded levels				
	−α	–1	0	+1	+α
Fe_3O_4@SiO_2-GO - X_1 (mg L^{-1})	1	6.87	15.5	24.12	30
Time - X_2 (min)	2	13.75	31	48.24	60
Initial Hg^{2+} Concentration - X_3 (ppb)	500	702.7	1000	1297	1500

2.8. Non-linear regression analysis

The optimization approaches can be improved by applying error functions in order to assess the fit of the model output values to the experimental results [29]. Table S2 presents the error functions which were applied as Goodness-of-Fit Measures (GoFMs).

3. Results and discussion

3.1. Characterization of Fe_3O_4@SiO_2-GO nanocomposite

The SEM image of GO represents many graphene nanosheets indicating the folding nature throughout the morphology (Fig. 2a) and that of Fe_3O_4@SiO_2-GO (Fig. 2b) reveals granular morphology having a granule size of 100–200 nm. Furthermore, Fig. S1 shows a typical TEM image of Fe_3O_4@SiO_2-GO exhibiting the spherical morphology of Fe_3O_4 nanoparticles with a diameter of approximately 30 nm having a well-distributed patterns throughout the GO sheets.

To characterize magnetic properties of synthesized materials, the vibration sample magnetization (VSM) was applied. As depicted in Fig. S2, the highest saturation magnetizations of Fe_3O_4, Fe_3O_4@SiO_2-NH_2, and Fe_3O_4@SiO_2-GO were 58.1, 43.2, and 24.4 emu g^{-1}, respectively. The magnetic decreasing is attributed to the consecutively covering of Fe_3O_4 nanoparticles by SiO_2-$NH_2$and GO layers leading to the formation of Fe_3O_4@SiO_2-GO nanocomposite. However, the residual saturation magnetization for Fe_3O_4@SiO_2-GO is 24.4 emu g^{-1}, which still is sufficient to separate the nanocomposite from the aqueous dispersion by applying an external magnetic field. The insert photographs of Fig. S2, show the effect of the external magnetic field on the nanocomposite separation. The dark yellow-brown hue of the

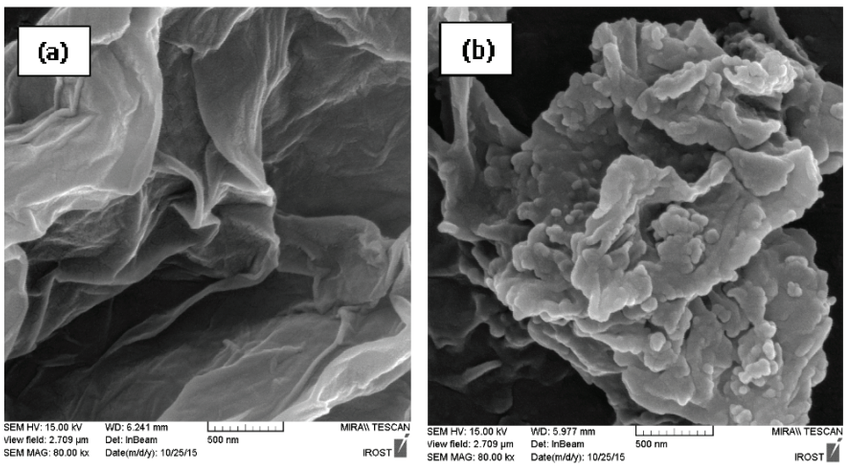

Fig. 2. Typical FE-SEM of GO (a), and Fe_3O_4@SiO_2-GO (b).

GO dispersion (Fig. S2; top-left image) confirms the occurrence of the oxygenation of GO nanosheets [30].

Fig. 3 illustrates a tapered mode AFM topography scan from GO sample containing an exfoliated GO nanosheets (Fig. 3a), a histogram of platelet thicknesses (Fig. 3b), and a height profile of the GO nanosheets (Fig. 3c). As is represented in Fig. 3c, the thickness of a GO flake is about 0.857 nm, which is attributed to the height profile indicated in Fig. 3a by a green line (Line 1). The obtained sub-nanometer thickness approves the synthesis of the GO monolayer [15].

The nitrogen adsorption isotherm of Fe_3O_4@SiO_2-GO is presented in Fig. S3. The surface area determined for the Fe_3O_4@SiO_2-GO is 270 m^2 g^{-1}. This relatively low specific surface area is probably due to the aggregation of Fe_3O_4 nanoparticles and graphene layers. The average pore size of Fe_3O_4@SiO_2-GO was determined to be about 9.26 nm identifying the mesopore structure of the adsorbent. As can be inferred from the isotherm (Fig. S3), the adsorption occurred in the low pressure region (<0.3 p/p_0) is relatively negligible. Also, formation of a hysteresis loop in the desorption branch identifies the formation of mesopore. In the pressure region beyond 0.85 p/p_0 , the adsorption trend was elevated sharply, revealing that the adsorption mainly occurs on the surface of GO nanosheets [31].

Obtained FTIR spectra of GO, Fe_3O_4, and Fe_3O_4@SiO_2-GO are illustrated in Fig. 4. The FTIR spectrum of GO contains the adsorption bands assigned to C–O stretching (1055 cm^{-1}), C–OH stretching (1226 cm^{-1}), and C–O carbonyl stretching (1733 cm^{-1}) [30]. Furthermore, the vibrations of O–H hydroxide stretching appeared at 3419 cm^{-1}. The stretching attributed to the adsorbed water molecules is detected at 1621 cm^{-1},which also can be assigned to the skeletal vibrations of un-oxidized graphite (Fig. 4a) [32].

Fig. 4b shows the spectrum of Fe_3O_4 nanoparticles, which the vibration of Fe-O stretching is revealed at 591 cm^{-1}. Moreover, an intense OH band around 3,400 cm^{-1} is detected which assigns both to the vibrations of Fe-OH stretching attached on the Fe_3O_4 surface and the remaining water on the surfaces of Fe_3O_4 nanoparticles [33].

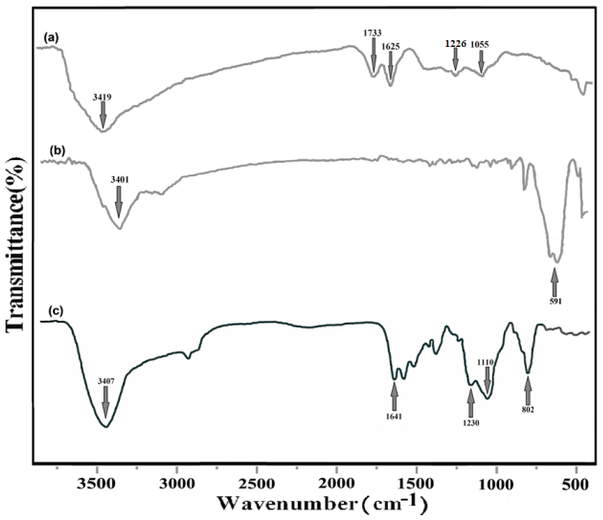

Fig. 4. FTIR spectra of GO (a), Fe_3O_4 magnetic nanoparticles (b), and Fe_3O_4@SiO_2-GO (c).

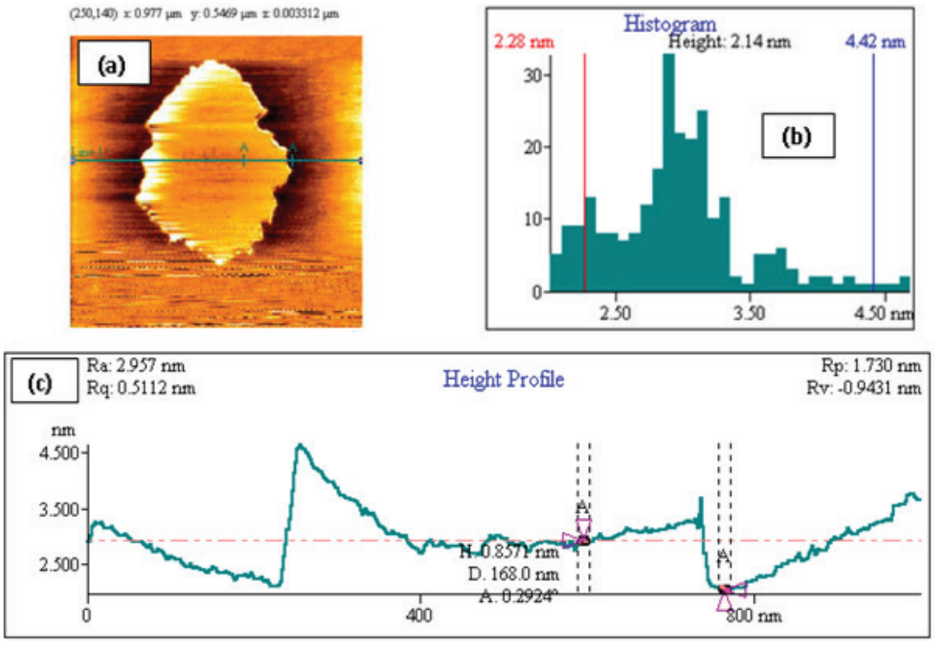

Fig. 3. Tapered mode AFM topography scan. Exfoliated graphene oxide deposited on a freshly cleaved mica surface (a). Histogram of platelet thicknesses from images of 260 platelets (the mean thickness is 2.14 nm) (b). Height profile through the green line (Line 1) presented in (a). Cross-section A-A through the sheet shown in (a) exhibiting a height minimum of 0.857 nm (c).

As shown in Fig. 4(c), the vibration of $–NH_2$ stretching is detected at 3401 cm^{-1}. The peak at 1733 cm^{-1}, which observed in Fig. 4a, has almost disappeared. In addition, a new wide peak assigned to C=O stretching of amide groups appears at 1641 cm^{-1}. The vibration of C–N stretching appears at 1230 cm^{-1} . Furthermore, as is revealed from Fig. 4c, the obvious peaks at 802 and 1110 cm^{-1} can be attributed to the Si–O vibrations. It can be concluded from the FTIR spectra that APTES functionalized Fe_3O_4 has been bonded covalently to GO nanosheets via the amide linkage [17].

As illustrated in Fig. S4, UV-visible spectrum of GO aqueous dispersion (the orange curve) shows a Plasmon peak at 231 nm which can be attributed to the transitions because of the aromatic bonds. Furthermore, a humpy pattern is detected around 300 nm assigning to the transitions of bonds. An aqueous solution containing mercury (II) ions was spiked gradually into the GO dispersion which creates a growing humpy arrangement around 300 nm. It corresponds to the formation of an Hg^{2+}-GO complex via bonds of carboxylic groups located on the edge of GO nanosheets.

Fig. S5 shows temperature gravimetric analysis (TGA) curves of Fe_3O_4 magnetic nanoparticles, Fe_3O_4@SiO_2-GO, and graphene oxide. The differences between profiles Fig. S5a and Fig. S5b corresponds to the sample weight loss assigned to the graphene oxide.

XRD patterns of GO and Fe_3O_4@SiO_2-GO are depicted in Fig. 5. Fig. 5a shows the GO sharp diffraction peaks at 2θ = 12.24° and 42.83° corresponding to the reflections of (002) and (101), respectively. Fig. 5b illustrates the XRD pattern of the Fe_3O_4@SiO_2-GO nanocomposite. As shown, six characteristic peaks are indicated at about 2θ = 30.4, 35.6, 43.1, 54.1, 57.7 and 62.5°, corresponding to their indices (220), (311), (400), (422), (511) and (440), respectively. Pure magnetite JCPDScard (75-1610) confirms the appropriate match of intensities and positions of above mentioned diffraction peaks [34]. As depicted in Fig. 5b, the reflection peak (002) of GO was disappeared. It seems that covering the GO sheets by Fe_3O_4 nanoparticles hinders stacking the sheets on top of one another to arrange a crystalline structure [34].

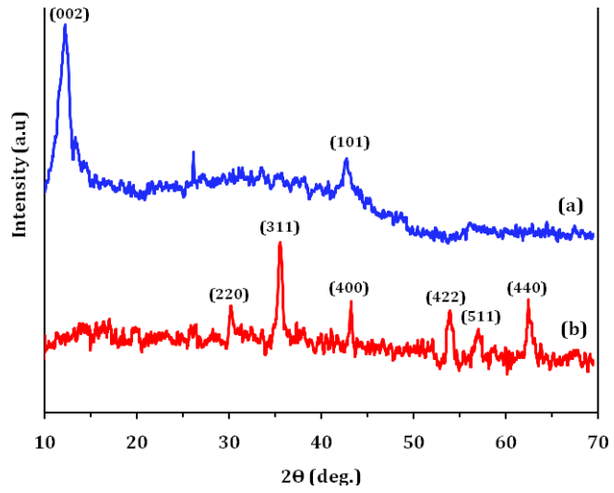

Fig. 5. XRD patterns of GO (a) and Fe_3O_4@SiO_2-GO(b).

3.2. Response surface methodology model analysis

A quadratic model by applying three factors can be found in Eq. (4).

$$\begin{aligned} &Mercury(II)Removal(\%) \\ &= 2.1X_1 + 1.53X_2 - 0.102X_3 - 0.05X_1X_2 - 0.0005X_1X_3 \\ &+0.0007X_2X_3 + 0.033X_1^2 - 0.009X_2^2 + 0.00004X_3^2 + 72.23 \end{aligned} \quad (4)$$

where X_1 is Fe_3O_4@SiO_2-GO dosage (mg L^{-1}), X_2 is contact time (min), and X_3 is mercury (II) concentration (mg L^{-1}). Table 2 shows the ANOVA analysis of mercury (II) removal using Fe_3O_4@SiO_2-GO nanocomposite. The value of multiple R^2 in Table 2 and Fig. 6 means 94.2 % of the variability in the response could be explained by the quadratic models. When various terms are presented in the model and also, when the sample size is not large, the adjusted R^2 can be considerably lower than Multiple R^2 [35]. In the current work, the adjusted R^2 is almost 91% confirming both the significance of model and satisfactory adjustment for the quadratic model to the experimental data [36].

As can be revealed from Table 3, the "lack of fit (LOF)" value was 0.878. The insignificant values of LOF (>0.05) and the significant P-values for the quadratic model show that, applied model is eligible to interpret the mercury (II) removal process [37].

Fig. 6 illustrates the values of removal efficiencies obtained from the laboratory experiments versus those obtained from the quadratic model presented in Eq. (4). These findings are in agreement with the reports of applied quadratic model in CCD [20,21,36].

Contour plots illustrated in Fig. 7 are the graphical depictions of Eq. (4) representing the simultaneous effects of adsorbent dosage-time (a), time- initial mercury (II) concentration (b), and adsorbent dosage - initial mercury (II)

Table 2
Analysis of variance (ANOVA) for the quadratic model

Model formula in RSM (X_1,X_2,X_3)	DF	Sum of squares	Mean square	F-value	Probability (P)
First-order response	3	4486.2	1495.41	73.08	0.0000
Two-way interactions	3	567.6	189.20	9.25	<0.0008
Pure quadratic response	3	404.9	134.96	6.59	<0.004
Residuals	16	327.4	20.46	–	–
Lack of fit	5	43.7	8.74	0.34	0.878*

Multiple R^2 = 0.942; Adjusted R^2 = 0.909; *Lack of fit: 0.878

concentration (c) on the mercury (II) removal efficiency as the response factor.

The interaction effects of Fe_3O_4@SiO_2-GO dose (X_1) and time (X_2) on the mercury (II) removal shown in Fig. 7a imply that at contact times more than 45 min, the mercury(II) ion removal efficiency was almost adsorbent dosage-free, and remained in amounts beyond 86%. Furthermore, at low contact times around 15 min, the increase in the adsorbent dosage from 7 to 24 mg L^{-1} could tend to increase the removal efficiency from 54% to 86% representing the noticeable impact of contact time on the removal efficiency

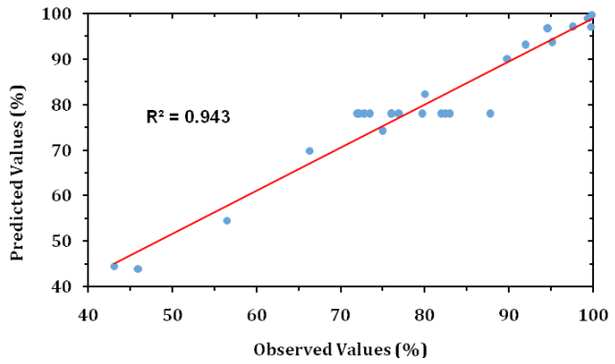

Fig. 6. Observed (experimental) values versus predicted values from quadratic model.

of mercury (II) ions in the aqueous solution. These findings revealed that the enhanced adsorption rate of mercury (II) over short contact time can be assigned to the high affinity of mercury (II) ions to hydroxide (–OH), epoxide (–O–) and carboxylic (–COOH) groups on the GO nanosheets [37,38].

Fig. 7b shows higher removal efficiencies obtained in lower mercury (II) ion initial concentrations at contact times less than 40 min. Furthermore, after contact times beyond 40 min, the removal efficiencies more than 85% have been acquired, which were almost independent from the mercury (II) initial concentration.

As is revealed from Fig. 7c, the removal efficiencies more than 83 percent can be achieved by applying Fe_3O_4@SiO_2-GO doses more than 20 mg L^{-1} for all mercury (II) initial concentrations. It may be assigned to the increased collisions between mercury (II) ions and the adsorbent nanosheets. Therefore, it might induce an increase in electrostatic interactions engaged with sites with lower affinity for mercury (II) ions [1,29].

The optimum values of Fe_3O_4@SiO_2-GO dosage (X_1), contact time (X_2), and initial mercury (II) concentration (X_3) were determined using Solver add-Ins in Microsoft Excel by applying the quadratic model obtained from RSM [Eq. (4)]. The optimum values were found to be 23 mg L^{-1}, 21 min, and 550 ppb for Fe_3O_4@SiO_2-GO dosage, contact time, and initial mercury (II) concentration, respectively. The pH study, and other investigations such as isotherm and kinetic experiments, were performed according to the optimum values derived from RSM model.

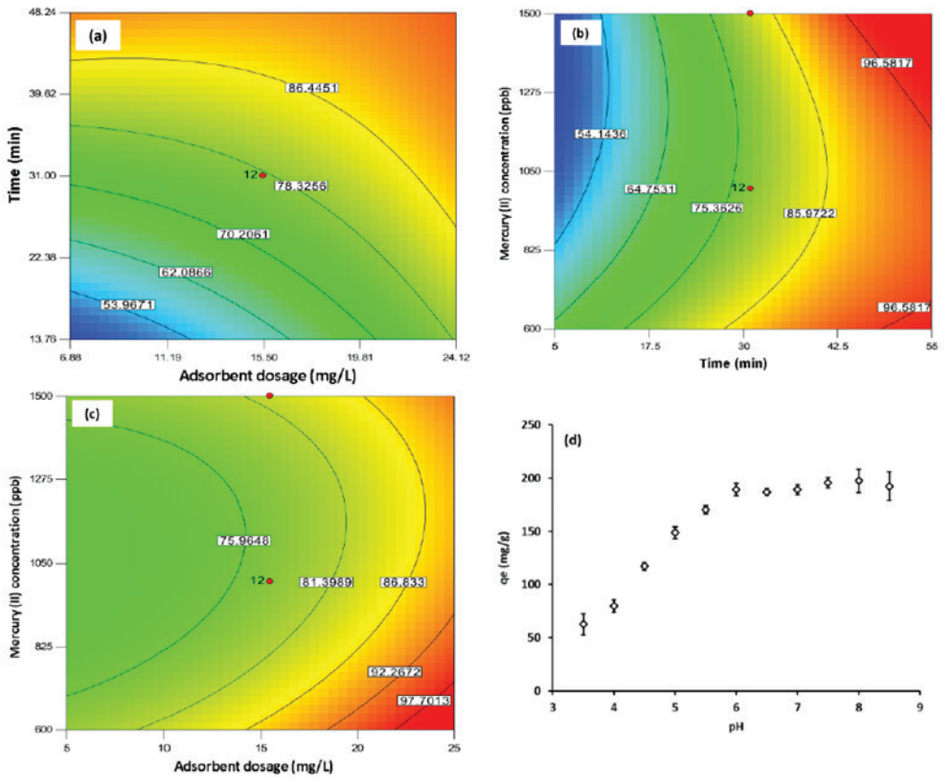

Fig. 7. Contour plots for the effect of factors on the mercury (II) removal. Adsorbent dosage vs. pH (a), contact time vs. mercury (II) concentration (b), adsorbent dosage vs. mercury (II) concentration (c), the effect of pH on the equilibrium adsorption (mg Hg(II)/g) (adsorbent dosage: 23 mg L^{-1}, C_0 (mercury): 550 ppb, contact time: 21 min, T = 298 K) (d).

3.3. pH study

The effect of pH on the mercury (II) removal was depicted in Fig. 7d. As is shown in this figure, the adsorption capacity was dramatically dropped by decreasing pH from 5.5. This may due to the effect of protonation which surrounds the active sites on the graphene oxide nanosheets and its competing with mercury (II) ions in site occupation [1,37].

3.4. Adsorption isotherms

In order to investigate the adsorption equilibrium of mercury (II), some isotherm models were applied. Table S3 presents the original (nonlinear) forms of isotherm models applied to fit with the experimental results.

Fig. 8 depicts the non-linear forms of the isotherm models fitted on the experimental results. The parameters of isotherm models can be observed in Table 3.

As shown in Table 3, the maximum adsorption capacity was obtained to be 355.4 mg g^{-1} according to the Langmuir q_m parameter.

Table 4 presents the isotherm models ranked by using the error functions. As can be observed, Sips isotherm model has better rank value and can be considered the appropriate model to fit with the experimental points. The Sips model includes three parameters and has the capability to apply to both the homogeneous and heterogeneous systems [39].

The Sips model (Eq. (S3)) integrates parameters from both the Langmuir and the Freundlich models. The heterogeneous surface of adsorbent can be identified if n_S value deviates from the unity [29]. However, the Sips isotherm moves toward a constant level at high concentrations whereas a pattern of Freundlich model can be observed at low concentrations [39].

According to the experimental data, the maximum adsorption capacity (q_m) was 328.3 mg g^{-1}, indicating the adsorption capacity to be higher than those reported by studies applying magnetic GO as mercury (II) adsorbent [38]. The maximum adsorption uptake (q_m) obtained from Sips isotherm model was found to be 569.3 mg g^{-1} which was more than the values achieved both from the Langmuir model and the experimental data ($q_{m,\text{Langmuir}}$ = 355.4 mg g^{-1}, $q_{m,\text{exp}}$ = 328.3 mg g^{-1}). As is observed, Sips model overestimates q_m value which can be assigned to the heterogeneity characteristic of Sips model [29]. As shown in Table 3, the n_S value deviates from the unity (n_S = 0.44) and the n_F value is more than unity (n_F = 3.78), which can be attributed to the crosslinking effects beside the amount of functionalities such as –COOH and –OH on the adsorbent surface (see FTIR-spectra in Fig. 6) [1,7]. The isotherm curves are L-shaped, showing the high affinity of surface groups towards mercury (II) ions both at low and high concentrations [29]. As is revealed from Table 3, the mean free energy E_{ads} is 11.9 KJ/mol, indicating the predomination of chemisorption mechanism [39].

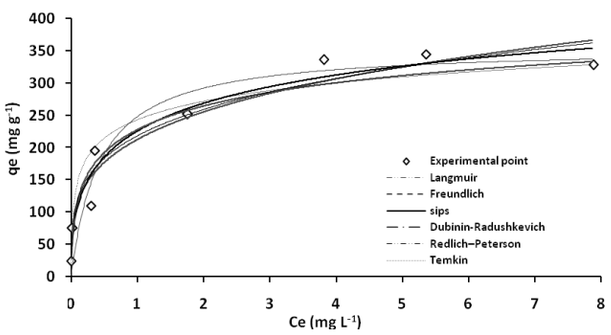

Fig. 8. Fitting results of different isotherms for mercury (II) adsorption by Fe_3O_4@APTES-GO (a), and inset table contains parameters obtained for the isotherm models (b). ($q_{m,exp}$: 328.3 mg g^{-1}, Adsorbent dosage: 23 mg L^{-1}, pH: 5, $C_{0,\text{Mercury(II)}}$: 0.5–15 mg L^{-1}, time : 21 min, T = 298 K).

3.5. Adsorption kinetics

Table S3 presents the nonlinear forms of three kinetic equations used to achieve the appropriate kinetic model having better fit with the experimental data.

Table S4 presents the regression coefficient values of applied kinetic models. It was found that the double exponential kinetic model (R^2 = 0.997) obtains better description to predict the kinetic experimental data of mercury (II) adsorption than both the pseudo-first-order and pseudo-second order models.

The values of constant parameters of double-exponential kinetic model(DEM) revealed that both the external diffusion and the internal diffusion have substantial effects on the mercury (II) sorption using Fe_3O_4@SiO_2-GO nano-

Table 3
The parameters of isotherm models

Isotherm model	Parameter	Unit	Value
Langmuir	R^2	–	0.926
	q_m	mg g^{-1}	355.4
	K_L	L/mg	2.303
Freundlich	R^2	–	0.944
	n_F	–	3.786
	K_F	mg g^{-1}	212.4
Sips	R^2	–	0.955
	q_m	mg g^{-1}	569.5
	K_s	L/mg	0.387
	n_s	–	0.444
Dubinin-Radushkevich	R^2	–	0.881
	q_m	mg g^{-1}	421.9
	B_{DR}	mol^2/J^2	3.5×10^{-9}
	E_{ads}	KJ/mol	11.901
Redlich-Peterson	R^2	–	0.948
	q_m	mg g^{-1}	220.45
	K_{RP}	L/mg	93.94
	n_{RP}	–	0.758
Temkin	R^2	–	0.903
	B_T	J/mmol	0.215
	A_T	L/mmol	73782.7

Table 4
Isotherm models ranked from the best to worst based on GoFM values for the removal of mercury

Rank	R^2	ERRSQ	SAE	ARE	ARS	MPSD	Most Visited
1	Sips	Sips	D-R	R-P	Sips	R-P	Sips
2	R-P	R-P	R-P	D-R	D-R	Sips	R-P*
3	D-R	D-R	Sips	Sips	R-P	D-R	D-R**
4	Freundlich	Freundlich	Freundlich	Freundlich	Temkin	Freundlich	Freundlich
5	Langmuir	Langmuir	Temkin	Langmuir	Freundlich	Langmuir	Langmuir
6	Temkin	Temkin	Langmuir	Temkin		Temkin	Temkin

*Redlich-Peterson, ** Dubinin-Radushkevich

composite [40]. Because K_{D1} is noticeably greater than K_{D2}, it reveals that the rapid process is negligible on the overall kinetics and Eq. (S16) can then be simplified as follows [40]:

$$q_t = q_e - \frac{D_2}{x_{ads}} \exp\left(-k_{D_2} t\right) \quad (5)$$

So, by rearranging Eq. (5), it can be used to plot the linear form of DEM kinetics. Although DEM was originally proposed to model Pb^{2+} and Cu^{2+}, it seems that DEM can describe the Hg^{2+} kinetic behavior better than pseudo- first and pseudo-second kinetics.

3.6. Regeneration and reusability

Determining the reusability of the adsorbent is an important factor for assessing its capability to use in the real condition where the adsorbent is exposed to the consecutive adsorption/desorption cycles. Generally, after ending the adsorption process, the desorption phase can be applied via low pH condition to release the Hg^{2+} cations from the adsorbent body into the washing solution. The point of zero charge (pH_{pzc}) indicates the climax of changing the surface charge of the adsorbent. As observed in Fig. 9, the pH_{pzc} is 4.1 for Fe_3O_4@SiO_2-GO nanocomposite, which indicates that applying pH < 4.1 is helpful for regeneration process.

25 mL of mercury (II) solution was mixed with an amount of Fe_3O_4@SiO_2-GO nanocomposite to obtain the final adsorbent dosage of 400 mg L^{-1}. pH was adjusted at 5 during the adsorption time (1 h). After the separation of the adsorbent using an external magnetic field, the residual concentration of mercury (II) in the solution was measured. Then, 25 mL of 0.1 M HCl was added into the separated adsorbent, and agitated gently for 3 h. The mercury ions were released into the HCl solution. Then, the adsorbent was separated via an external magnetic field and the mercury concentrations was measured in the remained washing solution. After several washings of the separated adsorbent by distilled water to obtain neutral pH, the above mentioned cycle was repeated four times.

The regeneration steps to investigate EDTA 0.01 M as desorption agent was performed like the above mentioned approach except for applying EDTA 0.01 M instead of HCl 0.1 M.

The following equation was applied to determine the desorption ratio, D (%):

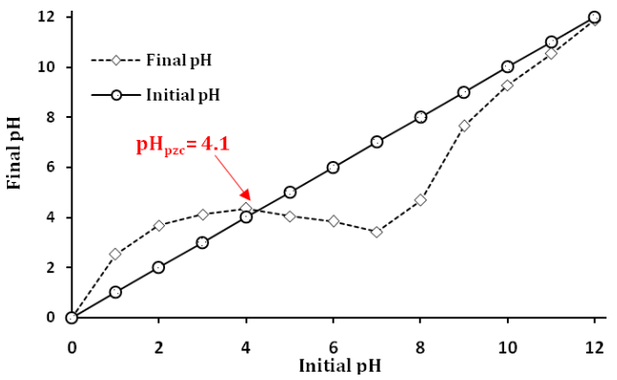

Fig. 9. Plotting the initial pH versus final pH to determine pH_{pzc} (Fe_3O_4@SiO_2-GO dosage: 0.4 g/L; Electrolit solution: NaCl 0.01 N; pH adjustment solutions: NaOH 0.1 M, HCl 0.1 M; Rest time to achieve final pH: 48 h; T: 298 K).

$$D(\%) = \frac{C_{desorbed}}{C_{adsorbed}} \times 100 \quad (6)$$

where $C_{desorbed}$ is concentration of mercury (II) in the washing solution , $C_{adsorbed}$ is the difference between initial (C_0) and final (C_e) concentrations during the adsorption process which can be found in Eq. (1).

Figs. 10 and 11 show the adsorption/desorption cycles performed by applying regeneration agents HCl 0.1 M and EDTA 0.01 M, respectively. As can be observed, for each regeneration agent (HCl 0.1 M or EDTA 0.01 M), the adsorption/desorption cycles were continued for 5 consecutive cycles.

As can be revealed from Figs. 10 and 11, using EDTA as an aliquot for the desorption process yields better efficiencies in the adsorption/desorption cycles than those obtained by HCl. The nanocomposite structure may be damaged when HCl is applied as the regeneration agent. It can be attributed to the vulnerability of nanocomposite structure in low pH condition made by HCl 0.1 M. As is depicted in Fig. 12, using HCl for the desorption process results in noticeable iron migration from the adsorbent structure. This can be assigned to the destructive effect occurred by the low pH condition, confirming the dramatically decrease of mercury (II) adsorption capacity illustrated in Fig. 10.

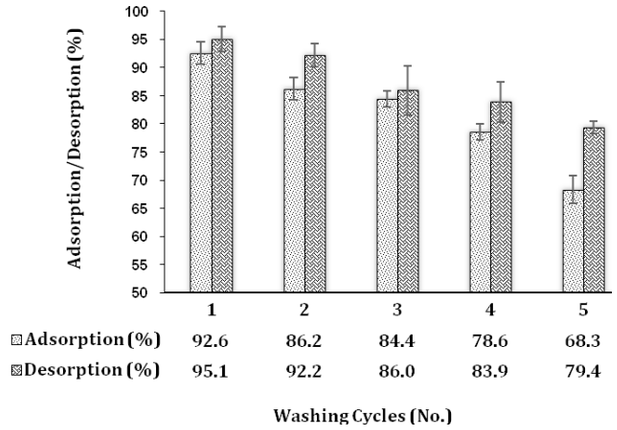

Fig. 10. Adsorption/desorption cycles by applying HCl 0.1 M.

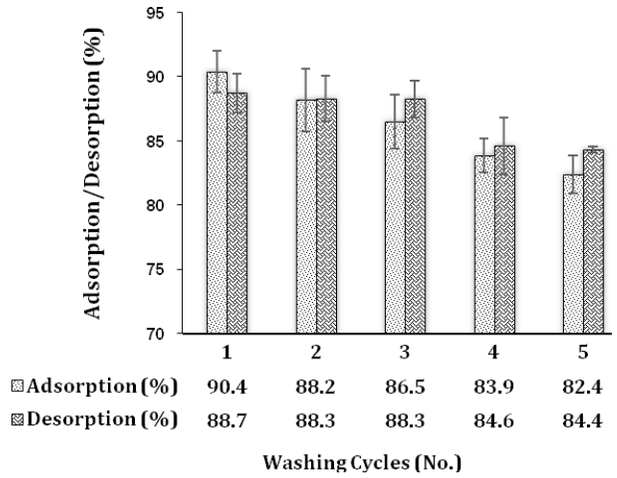

Fig. 11. Adsorption/desorption cycles by applying EDTA 0.01 M.

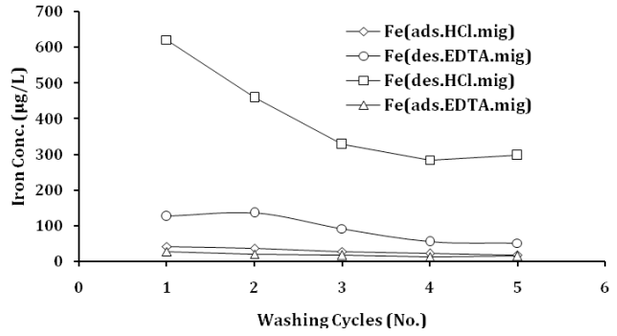

Fig. 12. Releasing (migration) the Iron from the Fe_3O_4@SiO_2-GO during the washing cycles (adsorption and desorption) using HCl and EDTA.

4. Conclusion

Magnetic Fe_3O_4@SiO_2-GO nanocomposite was fabricated and applied to eliminate the mercury (II) from aqueous solution. The removal process was found to be quick and facile, and the mercury (II) adsorption process was almost completed up to 21 min contact time.

Quick mercury separation by using external magnetic field and the noticeable mercury (II) removal (355 mg g^{-1}) were the prominent findings of the current study.

The results obtained from the analysis of response surface methodology indicates that time and adsorbent dosage were found to have significant effects on the removal efficiency of mercury (II). The optimization of process was performed and the experimental values were in agreement with the predicted values of the model.

The adsorption isotherms and kinetics were also investigated. Equilibrium adsorption data had the best fit by the Sips isotherm model and therefore, chemisorption mechanism was predominant. Kinetic studies indicated that the double-exponential kinetic model is the preferred model to explain the equilibrium adsorption over the time. The regeneration study shows that applying EDTA 0.01 M as a regeneration agent tends to obtain better results than HCl 0.1 M.

Acknowledgements

This research was part of a PhD dissertation by the first author and has been financially supported by a grant (NO, 28232-27-01-94) from Tehran University of Medical Sciences, Tehran, Iran. The authors would like to express their thanks to the Department of Environmental Health Engineering, School of Public Health, Tehran University of Medical Sciences for their collaboration.

Symbols

C_e — Equilibrium concentration of Hg^{2+} in solution (mg L^{-1})
C_0 — Initial concentration of Hg^{2+} in solution (mg L^{-1})
x_{ads} — Adsorbent dosage (g L^{-1})
R — The universal gas constant (J mol^{-1} K^{-1})
T — Temperature (K)
K_L — Langmuir adsorption constant (L mg^{-1})
K_F — Freundlich constant (mg g^{-1})
K_S — Sips affinity constant (L g^{-1})
K_1 — Pseudo-first-order constants
K_2 — Pseudo-second-order rate constants
K_{D2} — Diffusion parameter of the rapid step in DEM kinetics(min^{-1})
K_{D2} — Diffusion parameter of the rapid step DEM kinetics (min^{-1})
n — The number of experimental points
n_s — Sips the surface heterogeneity
n_F — Frendlich constant related to the heterogeneity factor
D_1 — Adsorption rate parameter of rapid step in DEM (mg L^{-1})
D_2 — Adsorption rate parameter of slow step in DEM (mg L^{-1})
$q_{e,\,exp}$ — The observed equilibrium adsorption (mg g^{-1})
$q_{e,\,calc}$ — The calculated equilibrium adsorption (mg g^{-1})
E_{ads} — Mean free energy of the adsorption per molecule
B_{DR} — Dubinin–Radushkevich model constant (mol^2/J^2)
ε — Polanyi potential
DEM — Double-exponential model kinetics

References

[1] V. Chandra, K.S. Kim, Highly selective adsorption of Hg^{2+} by a polypyrrole-reduced graphene oxide composite, Chem. Commun., 47 (2011) 3942–3944.

[2] A. Rahbar, S. Farjadfard, M. Leili, R. Kafaei, V. Haghshenas, B. Ramavandi, Experimental data of biomaterial derived from Malva sylvestris and charcoal tablet powder for Hg^{2+} removal from aqueous solutions, Data in Brief, 8 (2016) 132–135.

[3] EPA, Drinking Water Contaminants, in: National Primary Drinking Water Regulations, U.S. Environmental Protection Agency, 2015.

[4] R.F. Fard, A.A. Azimi, G.R.N. Bidhendi, Batch kinetics and isotherms for biosorption of cadmium onto biosolids, Desal. Water Treat., 28 (2011) 69–74.

[5] A. Jafari, A.H. Mahvi, S. Nasseri, A. Rashidi, R. Nabizadeh, R. Rezaee, Ultrafiltration of natural organic matter from water by vertically aligned carbon nanotube membrane, J. Environ. Health Sci. Eng., 13 (2015) 51.

[6] A. Jafari, A.H. Mahvi, H. Godini, R. Rezaee, S.S. Hosseini, Process optimization for fluoride removal from water by Moringa oleifera seed extract, Fluoride, 47 (2014) 152–160.

[7] A. Mehdinia, M. Akbari, T.B. Kayyal, M. Azad, High-efficient mercury removal from environmental water samples using di-thio grafted on magnetic mesoporous silica nanoparticles, Environ. Sci. Pollut. Res., 22 (2015) 2155–2165.

[8] M. Turan, U. Mart, B. Yüksel, M.S. Çelik, Lead removal in fixed-bed columns by zeolite and sepiolite, Chemosphere, 60 (2005) 1487–1492.

[9] M. Alvand, F. Shemirani, A Fe_3O_4@SiO_2@graphene quantum dot core-shell structured nanomaterial as a fluorescent probe and for magnetic removal of mercury(II) ion, Microchim. Acta, (2017) 1–9.

[10] A. Dalvand, E. Gholibegloo, M.R. Ganjali, N. Golchinpoor, M. Khazaei, H. Kamani, S.S. Hosseini, A.H. Mahvi, Comparison of Moringa stenopetala seed extract as a clean coagulant with alum and Moringa stenopetala-Alum hybrid coagulant to remove direct dye from textile wastewater, Environ. Sci. Pollut. Res., 23 (2016) 1–10.

[11] A. Dalvand, R. Nabizadeh, M.R. Ganjali, M. Khoobi, S. Nazmara, A.H. Mahvi, Modeling of Reactive Blue 19 azo dye removal from colored textile wastewater using L-arginine-functionalized Fe_3O_4 nanoparticles: Optimization, reusability, kinetic and equilibrium studies, J. Magn. Magn. Mater., 404 (2016) 179–189.

[12] S. Ghadiri, R. Nabizadeh, A. Mahvi, S. Nasseri, A. Mesdaghinia, S. Talebi, Potential of granulated modified nanozeolites Y for MTBE removal from aqueous solutions: Kinetic and isotherm studies, Pol. J. Chem. Technol., 14 (2012) 1–8.

[13] R. Rezaee, S. Nasseri, A. Mahvi, R. Nabizadeh, S. Mousavi, A. Rashidi, A. Jafari, S. Nazmara, Fabrication and characterization of a polysulfone-graphene oxide nanocomposite membrane for arsenate rejection from water, J. Environ. Health Sci. Eng., 13 (2015) 1–11.

[14] E. Aliyari, M. Alvand, F. Shemirani, Simultaneous separation and preconcentration of lead and cadmium from water and vegetable samples using a diethylenetriamine-modified magnetic graphene oxide nanocomposite, Anal. Methods, 7 (2015) 7582–7589.

[15] D.R. Dreyer, S. Park, C.W. Bielawski, R.S. Ruoff, The chemistry of graphene oxide, Chem. Soc. Rev., 39 (2010) 228–240.

[16] M. Alvand, F. Shemirani, Preconcentration of trace cadmium ion using magnetic graphene nanoparticles as an efficient adsorbent, Microchim. Acta, 181 (2014) 181–188.

[17] Y. Li, X.-Y. Wang, X.-P. Jiang, J.-J. Ye, Y.-W. Zhang, X.-Y. Zhang, Fabrication of graphene oxide decorated with Fe_3O_4@SiO_2 for immobilization of cellulase, J. Nanopart Res., 17 (2015) 1–12.

[18] M. Alvand, F. Shemirani, Fabrication of Fe_3O_4@graphene oxide core-shell nanospheres for ferrofluid-based dispersive solid phase extraction as exemplified for Cd(II) as a model analyte, Microchim. Acta, 183 (2016) 1749–1757.

[19] F. Chen, F. Yan, Q. Chen, Y. Wang, L. Han, Z. Chen, S. Fang, Fabrication of Fe_3O_4@SiO_2@TiO_2 nanoparticles supported by graphene oxide sheets for the repeated adsorption and photocatalytic degradation of rhodamine B under UV irradiation, Dalton Trans., 43 (2014) 13537–13544.

[20] M. Khazaei, S. Nasseri, M.R. Ganjali, M. Khoobi, R. Nabizadeh, A.H. Mahvi, S. Nazmara, E. Gholibegloo, Response surface modeling of lead(II) removal by graphene oxide-Fe_3O_4 nanocomposite using central composite design, J. Environ. Health Sci. Eng., 14 (2016) 1.

[21] H. Aslani, R. Nabizadeh, S. Nasseri, A. Mesdaghinia, M. Alimohammadi, A.H. Mahvi, N. Rastkari, S. Nazmara, Application of response surface methodology for modeling and optimization of trichloroacetic acid and turbidity removal using potassium ferrate(VI), Desalin. Water Treat., 57 (2016) 25317–25328.

[22] Y. Wen, J. Li, F. Yang, W. Zhang, W. Li, C. Liao, L. Chen, Salting-out assisted liquid–liquid extraction with the aid of experimental design for determination of benzimidazole fungicides in high salinity samples by high-performance liquid chromatography, Talanta, 106 (2013) 119–126.

[23] J. Li, R. Dong, X. Wang, H. Xiong, S. Xu, D. Shen, X. Song, L. Chen, One-pot synthesis of magnetic molecularly imprinted microspheres by RAFT precipitation polymerization for the fast and selective removal of 17[small beta]-estradiol, RSC Adv., 5 (2015) 10611–10618.

[24] W.S. Hummers Jr, R.E. Offeman, Preparation of graphitic oxide, J. Am. Chem. Soc., 80 (1958) 1339–1339.

[25] D.C. Marcano, D.V. Kosynkin, J.M. Berlin, A. Sinitskii, Z. Sun, A. Slesarev, L.B. Alemany, W. Lu, J.M. Tour, Improved synthesis of graphene oxide, ACS nano, 4 (2010) 4806–4814.

[26] L.J. Cote, F. Kim, J. Huang, Langmuir–Blodgett assembly of graphite oxide single layers, J. Am. Chem. Soc., 131 (2008) 1043–1049.

[27] M. Khoobi, T.M. Delshad, M. Vosooghi, M. Alipour, H. Hamadi, E. Alipour, M.P. Hamedani, Z. Safaei, A. Foroumadi, A. Shafiee, Polyethyleneimine-modified superparamagnetic Fe_3O_4 nanoparticles: An efficient, reusable and water tolerance nanocatalyst, J. Magn. Magn. Mater., 375 (2015) 217–226.

[28] P. Tartaj, C.J. Serna, Synthesis of Monodisperse Superparamagnetic Fe/Silica Nanospherical Composites, J. Am. Chem. Soc., 125 (2003) 15754–15755.

[29] E. Repo, EDTA-and DTPA-functionalized silica gel and chitosan adsorbents for the removal of heavy metals from aqueous solutions, in: Department of Energy and Environmental Technology, Lappeenranta University of Technology Laboratory of Green Chemistry, Mikkeli, Finland, 2011.

[30] S. Stankovich, D.A. Dikin, G.H. Dommett, K.M. Kohlhaas, E.J. Zimney, E.A. Stach, R.D. Piner, S.T. Nguyen, R.S. Ruoff, Graphene-based composite materials, Nature, 442 (2006) 282–286.

[31] M.S.L. Hudson, H. Raghubanshi, S. Awasthi, T. Sadhasivam, A. Bhatnager, S. Simizu, S. Sankar, O. Srivastava, Hydrogen uptake of reduced graphene oxide and graphene sheets decorated with Fe nanoclusters, Int. J. Hydrogen Energy, 39 (2014) 8311–8320.

[32] X. Sun, Z. Liu, K. Welsher, J.T. Robinson, A. Goodwin, S. Zaric, H. Dai, Nano-graphene oxide for cellular imaging and drug delivery, Nano Res., 1 (2008) 203–212.

[33] X. Yang, Y. Wang, X. Huang, Y. Ma, Y. Huang, R. Yang, H. Duan, Y. Chen, Multi-functionalized graphene oxide based anticancer drug-carrier with dual-targeting function and pH-sensitivity, J. Mater. Chem., 21 (2011) 3448–3454.

[34] E. Aliyari, M. Alvand, F. Shemirani, Modified surface-active ionic liquid-coated magnetic graphene oxide as a new magnetic solid phase extraction sorbent for preconcentration of trace nickel, RSC Adv., 6 (2016) 64193–64202.

[35] R.H. Myers, D.C. Montgomery, C.M. Anderson-Cook, Response surface methodology: process and product optimization using designed experiments, John Wiley & Sons, Hoboken, New Jersey, 2009.

[36] H. Turkyilmaz, T. Kartal, S.Y. Yildiz, Optimization of lead adsorption of mordenite by response surface methodology: characterization and modification, J. Environ. Health Sci. Eng., 12 (2014) 5.

[37] J. Bao, Y. Fu, Z. Bao, Thiol-functionalized magnetite/graphene oxide hybrid as a reusable adsorbent for Hg^{2+} removal, Nanoscale Res. Lett., 8 (2013) 1–6.
[38] L. Cui, Y. Wang, L. Gao, L. Hu, L. Yan, Q. Wei, B. Du, EDTA functionalized magnetic graphene oxide for removal of Pb(II), Hg(II) and Cu(II) in water treatment: Adsorption mechanism and separation property, Chem. Eng. J., 281 (2015) 1–10.
[39] E. Repo, J.K. Warchoł, A. Bhatnagar, M. Sillanpää, Heavy metals adsorption by novel EDTA-modified chitosan–silica hybrid materials, J. Colloid Interface Sci., 358 (2011) 261–267.
[40] H. Qiu, L. Lv, B.-c. Pan, Q.-j. Zhang, W.-m. Zhang, Q.-x. Zhang, Critical review in adsorption kinetic models, J. Zhejiang Univ., Sci., A, 10 (2009) 716–724.

Supplementary Material

Table S1
Observed and predicted values for the quadratic model

Run no.	Fe_3O_4@SiO_2-GO (mg L^{-1})	Tim (min)	Initial Hg^{2+} concentration (ppb)	Observed values (%)	Predicted values (%)	Residual
1	15.5	31.0	1000	72.9	77.9	–5
2	6.9	48.2	1297	99.8	97.1	2.7
3	15.5	31.0	1000	77	77.9	–0.9
4	24.1	13.8	703	89.9	90.1	–0.2
5	15.5	31.0	1000	76	77.9	–1.9
6	24.1	13.8	1297	75	74.1	0.9
7	15.5	31.0	1000	72.1	77.9	–5.7
8	6.9	48.2	703	95.2	93.6	1.6
9	15.5	31.0	1000	82	77.9	4.1
10	6.9	13.8	703	56.5	54.6	1.9
11	24.1	48.2	1297	97.6	97	0.6
12	6.9	13.8	1297	46	44	2
13	15.5	31.0	1000	79.7	77.9	1.8
14	24.1	48.2	703	99.5	99	0.5
15	15.5	60.0	1000	94.7	96.6	–1.9
16	15.5	31.0	1000	87.8	77.9	10
17	15.5	2.0	1000	43.1	44.5	–1.4
18	15.5	31.0	500	92	93	–1
19	15.5	31.0	1000	82.5	77.9	4.6
20	15.5	31.0	1000	73.5	77.9	–4.4
21	15.5	31.0	1500	80	82.4	–2.4
22	15.5	31.0	1000	72.3	77.9	–5.5
23	1.0	31.0	1000	66.3	69.9	–3.6
24	15.5	31.0	1000	83	77.9	5.1
25	15.5	31.0	1000	76	77.9	–1.9
26	30.0	31.0	1000	99.9	99.7	0.2

Table S2
Statistical Goodness-of-Fit Measures (GoFMs)

Definition	Error function	Equation no.
Sum of the square of the errors	$ERRSQ = \sum_{i=1}^{n} \left(q_{e,\exp} - q_{e,calc}\right)_i^2$	S9
Marquardt's percent standard deviation	$MPSD = \sum_{i=1}^{n} \left(\frac{q_{e,\exp} - q_{e,calc}}{q_{e,\exp}}\right)_i^2$	S10
Sum of absolute errors	$SAE = \sum_{i=1}^{n} \left\lvert q_{e,\exp} - q_{e,calc} \right\rvert_i$	S11
Average relative error	$ARE = \frac{\left(\sum_{i=1}^{n} \left\lvert \left(q_{e,\exp} - q_{e,calc}\right) / q_{e,\exp} \right\rvert\right)}{n}$	S12
Average relative standard error	$ARS = \sqrt{\frac{\sum_{i=1}^{n} \left[\left(q_{e,\exp} - q_{e,calc}\right) / q_{e,\exp}\right]^2}{n}}$	S13

Table S3
The equations of isotherm models

Model name	Equation	Equation no.
Langmuir	$q_e = \frac{q_m K_L C_e}{1 + K_L C_e}$	S1
Freundlich	$q_e = K_f C_e^{1/n_F}$	S2
Sips	$q_e = \frac{q_m (K_S C_e)^{n_S}}{1 + (K_S C_e)^{n_S}}$	S3
Dubinin-Radushkevich	$q_e = q_m \exp(-B_{DR}\epsilon^2)$	S4
	$\epsilon = RTln\left(1 + \frac{1}{C_e}\right)$	S5
	$E_{ads} = \frac{1}{\sqrt{2B_{DR}}}$	S6
Redlich-Peterson	$q_e = \frac{q_m K_{RP} C_e}{1 + (K_{RP} C_e)^{n_{RP}}}$	S7
Temkin	$q_e = \frac{RT}{b_T} \ln(A_T C_e)$	S8

Table S4
The equations of kinetic models

Model name	Equation	Equation no.
Pseudo-first-order	$q_t = q_e(1 - \exp(-k_1 t))$	S14
Pseudo-second-order	$q_t = \frac{K_2 q_e^2 t}{1 + q_e k_2 t}$	S15
Double-exponential	$q_t = q_e - \frac{D_1}{x_{ads}} \exp(-k_{D_1} t) - \frac{D_2}{x_{ads}} \exp(-k_{D_2} t)$	S16

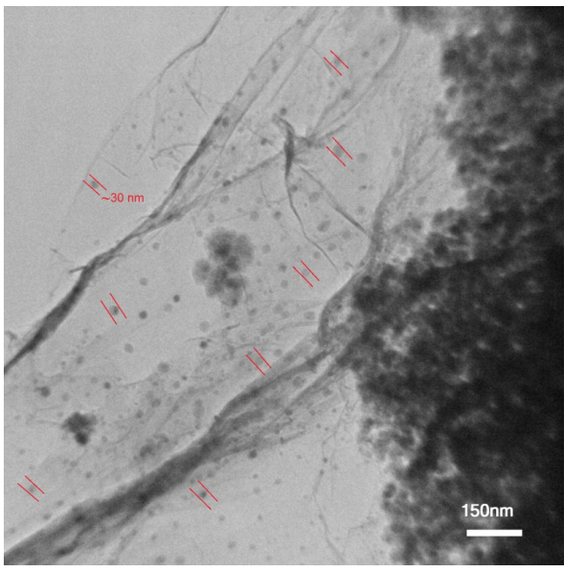

Fig. S1. Typical TEM image of Fe_3O_4@SiO_2-GO nanosheets.

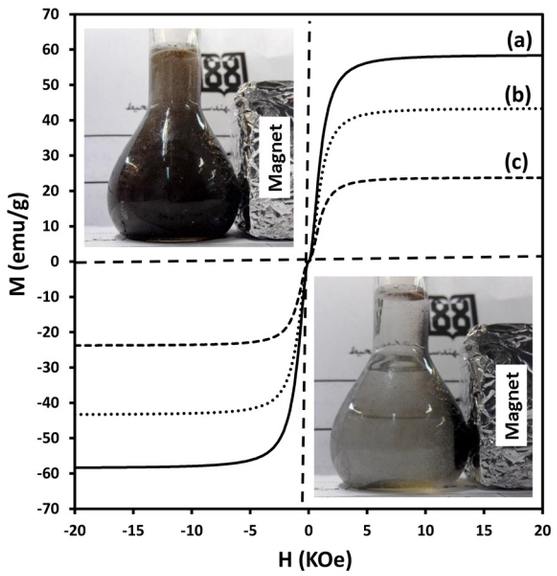

Fig. S2. Magnetic hysteresis loops of Fe_3O_4 (a), Fe_3O_4@SiO_2-NH_2 (b), and Fe_3O_4@SiO_2-GO (c). The inset photographic images show 1.4 mg mL^{-1} Fe_3O_4@SiO_2-GO dispersions in water, before (up-left image; t = 1 s) and after (down-right image; t = 15 s) exposing to an external magnetic field (d).

Table S5
Kinetic parameters of mercury (II) sorption onto the Fe_3O_4@SiO_2-GO

Pseudo-first-order		Pseudo-second-order		Double-exponential kinetic			
R^2	0.993	R^2	0.987	R^2	0.997	K_{D1} (min^{-1})	7.72
q_e (mg g^{-1})	89.07	q_e (mg g^{-1})	99.92	q_e (mg g^{-1})	89.92	D_2 (mg L^{-1})	1.88
K_1 (min^{-1})	0.113	K_2 (g mg^{-1} min^{-1})	0.0015	D_1 (mg L^{-1})	0.183	K_{D2} (min^{-1})	0.097

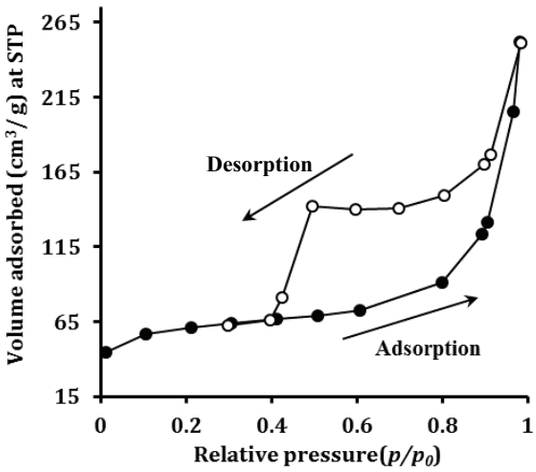

Fig. S3. Nitrogen adsorption–desorption isotherms for Fe_3O_4@SiO_2-GO nanocomposite.

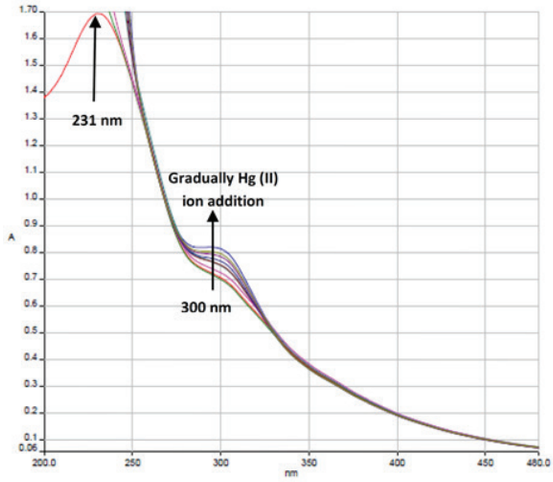

Fig. S4. UV-visible spectra for GO dispersion in water before (Orange curve) and after adding the different molar concentrations of mercury (II). (Hg (II) initial concentration = 1 µM, pH = 5, T = 298 K).

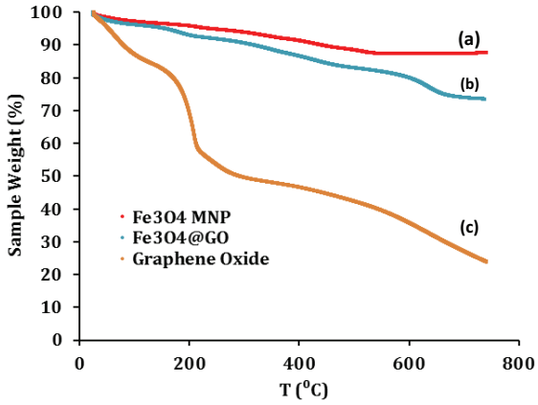

Fig. S5. The TGA curves of Fe_3O_4 magnetic nanoparticles (a), Fe_3O_4@SiO_2-GO (b), and graphene oxide (c).